Heliyon

ELSEVIER

Received:
1 November 2018
Revised:
2 February 2019
Accepted:
28 March 2019

Cite as: Misbah Ijaz, Muhammad Ayub. Simulation of magnetic dipole and dual stratification in radiative flow of ferromagnetic Maxwell fluid.
Heliyon 5 (2019) e01465.
doi: 10.1016/j.heliyon.2019.e01465

Simulation of magnetic dipole and dual stratification in radiative flow of ferromagnetic Maxwell fluid

Misbah Ijaz*, Muhammad Ayub

Department of Mathematics, Quaid-I-Azam University 45320, Islamabad 44000, Pakistan

* Corresponding author.

E-mail address: misbahijaz@math.qau.edu.pk (M. Ijaz).

Abstract

Theoretical investigation is performed to explore the novel aspects of nonlinear thermal radiation and non-uniform heat source/sink for chemically reactive flow of ferromagnetic Maxwell liquid over a permeable stretching sheet. Buongiorno model is employed to include Brownian motion and thermophoresis effects. The novelty of the existing study is to account the effect of binary chemical reaction, viscous dissipation, thermal and solutal stratification for ferromagnetic Maxwell fluid. Governing system of nonlinear partial differential equations is transformed into a system of nonlinear ordinary differential equations with the help of apposite similarity transformations. The acquired resulting nonlinear ODEs are solved numerically with the assistance built-in-shooting method (bvp4c). Effects of emanating variables are examined through graphs and tables. It is evident that heat transfer rate enhances with thermal radiation. It is analyzed that temperature upsurges for greater estimations of thermal radiation (N_1^*), ferromagnetic $(\widehat{\beta}_2)$ and thermophoresis $(\widehat{N}_t)$ parameters however it declines for Prandtl number (Pr) and thermal stratified parameter (S_1). Space and temperature dependent heat sinks are more appropriate for cooling purposes.

Keywords: Computational mathematics, Electromagnetism

https://doi.org/10.1016/j.heliyon.2019.e01465

1. Introduction

Thermal radiation is electromagnetic radiation produced by the thermal motion of particles in matter. All matter with a temperature greater than absolute zero emanates thermal radiation. The significance of this is that radiation will be the most effective mechanism for heat transfer whenever a vacuum is present. The rate at which a body radiates or absorbs thermal radiation relies on the nature of the surface as well. According to the statement Kirchhoff's radiation law, "objects that are good emitters are also good absorbers". A blackened surface is an excellent emitter as well as an excellent absorber. A blackbody is an idealized physical body that absorbs all the radiant energy in all frequencies that falls on it.

Sunlight also identified as solar radiation is a type of radiation that acquired from the sun. Sun/solar energy never run out, no burning or motions are required in the energy conservation procedure. Radiation effect has numerous applications in industry, physics and engineering like space technology, gas turbines, polymer processing, nuclear reactors, glass production, satellites and space vehicles. Initially, Pantokratoras [1] examined the consequence of linear and nonlinear Rosseland radiation on laminar natural convection beside a vertical isothermal plate using an innovative radiation parameter entitled as film radiation parameter. Mushtaq et al. [2] performed a heat transfer analysis in view of nonlinear thermal radiation via Rosseland approximation over a stretched surface. Krishnamurthy et al. [3] deliberated the features of linear thermal radiation on Williamson nanofluid model over a stretching sheet with chemical reaction impacts. Cortell [4] executed a numerical process for boundary layer problem in a quiescent fluid over a flat plate in the presence of nonlinear Rosseland thermal radiation. Mabood et al. [5] explored the effects of thermal radiation, variable thermal conductivity and non-uniform heat sources/sink for flow of a micropolar fluid over a stretching sheet embedded in a non-Darcian porous medium. Few modern investigations on radiative flow can be found in Refs. [6, 7, 8].

Stratification of fluid is composition/deposition of layers that appears due to the existence of dissimilar liquids or variations in temperature and concentration. The influence of stratification is vital in many energy storage systems and heat rejection process. In viable conditions where warmth and mass transfer run in parallel, it winds up essentially to analyse the impact of dual stratification on the nanofluids. Stratified liquids are bountiful in nature, i.e., heat release into the environment, for example, oceans and rivers, storage frameworks for thermal energy such as solar ponds, lakes, exchange of heat from warm sources such as the condensers of synthetic plants, groundwater reservoirs and seas, and various comparative examples. Several studies under different physical aspects have been reported in this direction. Hayat et al. [9] deliberated the influence of thermal stratification on steady mixed convective flow of Maxwell fluid. Ijaz et al. [10] studied the phenomena of thermal

https://doi.org/10.1016/j.heliyon.2019.e01465

and solutal stratification for ferromagnetic Maxwell nanofluid with non-uniform heat source/sink and viscous dissipation. Ibrahim and Makinde [11] considered the mixed convection flow of nanofluid with dual stratification. Ijaz et al. [12] explored the nonlinearly convective flow of Maxwell nanomaterial in presence of double stratification, non-uniform heat source/sink and activation energy. Hayat et al. [13] analyzed and modeled the duly stratified mixed convective flow of Jeffrey fluid with heat thermal radiation impacts. Srinivasacharya and Surender [14] characterized dual stratification in mixed convection flow of viscous nanoliquid embedded through porous medium. Hayat et al. [15] discussed MHD nanofluid flow with thermal and solutal stratification.

Ferrofluids characterize a special class of magnetizable fluids with fascinating properties fit for significantly impact on technology. Ferrofluid (FF), is a colloidal suspension of single-domain magnetic particles, with typical dimensions of about 10 nm, dispersed in a liquid carrier. They are frequently used in many industrial application, food preserving, aerodynamics, nuclear power plants, crystal processing, laser, avionics, robotics, cooling agent, semiconductor processing, fiber optics, loudspeakers, refrigeration, filtration, drawing plastic, aerodynamics and computer peripherals etc. Due to these innumerable applications, many researchers and scientists accelerated the study of ferrofluids. Primarily, Anderson and Vanes [16] examined the special effects of magnetic dipole on ferrofluid. Zeeshan et al. [17] investigated the combine effects of radiation and magnetic dipole in flow of viscous ferroliquid. Zubair et al. [18] discussed modified Fourier law in presence of magnetic dipoles for flow problem of ferromagnetic Powell-Eyring fluid. Thermally stratified flow of second grade ferrofluid in view of magnetic dipole and viscous dissipation is discussed by Muhammad et al. [19]. Hayat et al. [20] explored the impacts of thermal radiation and magnetic dipole in flow of ferromagnetic Williamson liquid over a stretched surface. Some significant work related to ferrofluid can be viewed via refs. [21, 22, 23, 24, 25].

The study of heat and mass transfer with chemical reactions are of great significance in many applications for example drying, polymer production, distribution of temperature and moisture over farming fields and forests of natural product trees, damage of crops due to freezing, evaporation at the surface of a water body and energy transfer in a wet cooling tower and stream in a desert cooler. Chamka et al. [26] deliberated the response of chemical reaction on free convective heat and mass transfer on a stretching sheet embedded in a porous medium. Pal and Mondal [27] inspected the mutual effects of non-uniform heat source/sink and thermal radiation in the presence of suction/injection on unsteady boundary layer flow of an incompressible viscous fluid over a porous vertical plate. The impact of chemical reaction on unsteady flow of a micropolar fluid over a stretching sheet through a non-Darcian porous space was examined by Srinivas et al. [28]. The impacts of magnetic field and chemical reaction for flow of couple stress fluid over a non-linearly stretching sheet are studied by Khan et al. [29].

https://doi.org/10.1016/j.heliyon.2019.e01465

In the present study, nonlinear radiative flow of Maxwell ferrofluid under the influence of magnetic dipole is considered over a linearly permeable stretched sheet. The novel binary chemical reaction model is employed with viscous dissipation, non-uniform heat source/sink and dual stratification. Highlights of Brownian movement and thermophoresis are explored within the sight of magnetic dipole. Features of thermal and concentration stratification are additionally examined. Problem is formulated and then solved numerically by built-in bvp4c package which uses the Collocation method [30, 31]. The achieved results are comprehensively discussed through graphs and tables.

2. Model

Two-dimensional, incompressible flow of ferromagnetic Maxwell fluid [32] with non-uniform heat generation and nonlinear thermal radiation over a permeable elastic sheet in the presence of magnetic dipole is analyzed. The direction of magnetic field is taken in the positive x-direction that develops a magnetic field of ample strength to saturate the ferrofluid. Features of nonlinear thermal radiation, non-uniform heat generation/absorption, Brownian motion, thermophoresis and viscous dissipatin are also accounted for present flow situation. Two equal and opposite forces are applied along the x-axis to produce the stretching velocity of the form $U_w(= d_2 x_1)$, which is directly proportional to the distance from the fixed origin. Further, magnetic dipole of adequate strength is positioned at some distance (b) below the x-axis and centered at y-axis (see Fig. 1). Temperature and concentration of ferroliquid at sheet are (T_w) and (C_w) respectively while relationship $T_\infty < T_w < T_c$ between ambient and Curie temperature holds. The Cauchy stress tensor for the Maxwell fluid model is presented in Eq. (1).

$$\boldsymbol{T} = -\boldsymbol{P}\boldsymbol{I} + \boldsymbol{\tau}, \tag{1}$$

$$\boldsymbol{\tau} + \Gamma_1 \frac{D\boldsymbol{\tau}}{Dt} = \widehat{\mu}\boldsymbol{A}_1, \tag{2}$$

Where $\boldsymbol{A}_1(= \boldsymbol{L} + \boldsymbol{L}^{T^*})$ denotes the first Rivlin−Ericksen tensor, $(\boldsymbol{P})$ the fluid pressure, $(\boldsymbol{\tau})$ the extra stress tensor $(Eq.\ (2))$, $(\widehat{\mu})$ the dynamic viscosity, $\left(\frac{D\tau}{Dt}\right)$ the upper-convected derivative of the tensor and (Γ_1) fluid relaxation time respectively.

The momentum expression (Eq. (3)) is

$$\widehat{\rho}\frac{d\boldsymbol{V}}{dt} = \nabla.\boldsymbol{\tau} - \nabla\mathbf{P}, \tag{3}$$

https://doi.org/10.1016/j.heliyon.2019.e01465

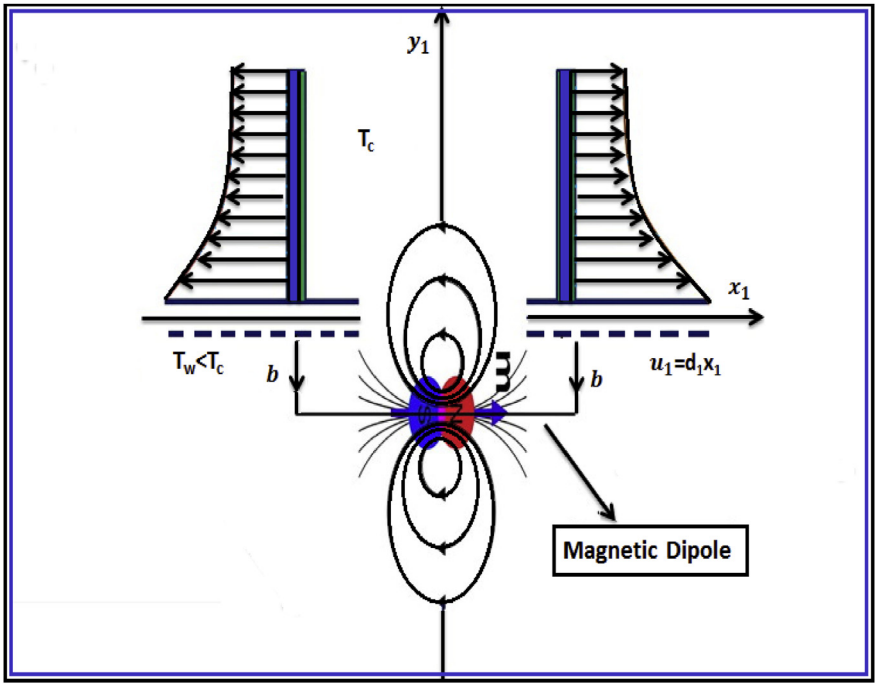

Fig. 1. Flow geometry.

The incompressibility constraint (Eq. (4)) and the constitutive law (Eq. (5)) is of the following form

$$\nabla.\boldsymbol{V}=0, \tag{4}$$

$$(\boldsymbol{V}.\nabla)\boldsymbol{\tau}-(\nabla\mathbf{V})\boldsymbol{\tau}-\boldsymbol{\tau}(\nabla\mathbf{V})^{T^*}+\Gamma_1\boldsymbol{\tau}=\widehat{\mu}\left[(\nabla\mathbf{V})+(\nabla\mathbf{V})^{T^*}\right], \tag{5}$$

The governing flow expressions for present model after applying above-mentioned expressions in view of boundary layer approximations are Eqs. (6), (7) and (8).

$$\left.\begin{aligned}\mathrm{w}_1\frac{\partial \mathrm{w}_1}{\partial \mathrm{x}_1}+\mathrm{v}_1\frac{\partial \mathrm{w}_1}{\partial \mathrm{y}_1}=\nu_1\frac{\partial^2 \mathrm{w}_1}{\partial \mathrm{y}_1^2}\frac{\Gamma_1}{\widehat{\rho}}\left(\mathrm{w}_1^2\frac{\partial^2 \mathrm{w}_1}{\partial \mathrm{x}_1^2}+2\mathrm{w}_1\mathrm{v}_1\frac{\partial^2 \mathrm{w}_1}{\partial \mathrm{x}_1\partial \mathrm{y}_1}+\mathrm{v}_1^2\frac{\partial^2 \mathrm{w}_1}{\partial \mathrm{y}_1^2}\right)\\ +\frac{\varsigma_o \mathrm{M}^*}{\widehat{\rho}}\frac{\partial \widehat{\boldsymbol{H}}_1}{\partial \mathrm{x}_1},\end{aligned}\right\} \tag{6}$$

$$\left.\begin{aligned}w_1\frac{\partial T}{\partial x_1}+v_1\frac{\partial T}{\partial y_1}+\frac{\varsigma_o T}{\widehat{\rho}}\frac{\partial M^*}{\partial T}\left(w_1\frac{\partial \widehat{\boldsymbol{H}}_1}{\partial x_1}+v_1\frac{\partial \widehat{\boldsymbol{H}}_1}{\partial y_1}\right)=\alpha^*\frac{\partial^2 T}{\partial y_1^2}-\frac{\partial \widehat{q}_r}{\partial y_1}\\ +\frac{Q_m}{(\widehat{\rho}C_p)_f}+\tau_1^*\left(\widehat{D}_B\frac{\partial \mathrm{C}}{\partial y_1}\frac{\partial T}{\partial y_1}+\frac{\widehat{\mathrm{D}}_T}{T_\infty}\left(\frac{\partial T}{\partial y_1}\right)^2\right)+\frac{\widehat{\mu}}{(\widehat{\rho}C_p)_f}\left(\frac{\partial w_1}{\partial y_1}\right)^2,\end{aligned}\right\} \tag{7}$$

https://doi.org/10.1016/j.heliyon.2019.e01465

$$w_1\frac{\partial C}{\partial x_1}+v_1\frac{\partial C}{\partial y_1}=\widehat{D}_B\frac{\partial^2 C}{\partial y_1^2}+\frac{\widehat{\mathrm{D}}_T}{T_\infty}\frac{\partial^2 T}{\partial y_1^2}-K_2(C-C_\infty), \tag{8}$$

Here, 3^{rd} terms on the right-hand side of Eq. (6) signify the magnetic body force per unit volume $(\varsigma_o M^*\nabla\widehat{\boldsymbol{H}}_1)$, and 2^{nd} term on the left-hand side of energy Eq. (7) accounts for heating due to adiabatic magnetization. Further, $(\mathrm{w}_1,\mathrm{v}_1)$ symbolize for the velocity components along x_1 and y_1 directions, (ς_o) for magnetic permeability, (M^*) for the magnetization, $(\widehat{\boldsymbol{H}}_1)$ for magnetic field, $(\widehat{\rho})$ fluid density, (α^*) the thermal diffusivity of liquid, $(\widehat{q}_r)$ the component of radiative flux (q), (τ_1^*) the specific heat ratio, (C_p) for the specific heat, (K_2) for reaction rate constant while $\mathrm{K}_2>0$ leads to destructive and $\mathrm{K}_2<0$ for generative chemical reactions, $(\widehat{\mathrm{D}}_\mathrm{B})$ Brownian diffusion coefficient and $(\widehat{\mathrm{D}}_\mathrm{T})$ for thermophoretic diffusion coefficient respectively.

The boundary conditions are defined in Eqs. (9) and (10)

$$w_1=U_w=d_2x_1,\ v_1=V_p,\ T=T_w=T_o+\widehat{e}_1x_1,\ \mathrm{C}=\mathrm{C}_w=\mathrm{C}_o+\widehat{e}_3x_1\ \ at\ y_1=0, \tag{9}$$

$$\mathrm{w}_1\to 0,\ \mathrm{v}_1\to 0,\ \mathrm{T}\to T_\infty=T_o+\widehat{\mathrm{e}}_2\mathrm{x}_1,\ \mathrm{C}\to\mathrm{C}_\infty=\mathrm{C}_\mathrm{o}+\widehat{\mathrm{e}}_4\mathrm{x}_1\ \ \text{when}\ \mathrm{y}_1\to\infty, \tag{10}$$

Here, V_p indicates the uniform surface mass flux, where $V_p<0$ corresponds to suction and $V_p>0$ corresponds to injection. Moreover, (U_w) signifies for stretching velocity, (T,C) for fluid temperature and solid nanoparticle volume fraction, $(d_2,\widehat{e}_1,\widehat{e}_2,\widehat{e}_3,\widehat{e}_4)$ for the dimensional constants, (T_o,C_o) for reference temperature and concentration, respectively.

Non-uniform heat source/sink Q_m [33] is defined in Eq. (11)

$$Q_m=\frac{U_w(x_1)k^*}{x_1\nu}\left[\widehat{B}_1(T_w-T_o)\frac{\partial \mathrm{F}}{\partial\eta}+\widehat{B}_2(T-T_\infty)\right], \tag{11}$$

Where $(\widehat{B}_1,\widehat{B}_2)$ designates the coefficients of heat generation/absorption depending on space and temperature, respectively. The positive values of $\widehat{B}_1$ and $\widehat{B}_2$ signify the internal heat generation, while negative standards represent the internal heat absorption.

Instead of the linearized Rosseland approximation, we use nonlinear Rosseland diffusion approximation from which one can attain results for both small and large differences between T_w and T_∞. According to Rosseland approximation for radiation [34, 35, 36], the radiative heat flux $\widehat{\mathrm{q}}_\mathrm{r}$ (Eq. (12)) in simplified form is

$$\widehat{q}_r=-\frac{4\tilde{\sigma}}{3\dot{k}}\frac{\partial T^4}{\partial y_1}=-\frac{16\tilde{\sigma}T_c^3}{\dot{k}}\frac{\partial T}{\partial y_1}, \tag{12}$$

https://doi.org/10.1016/j.heliyon.2019.e01465

Where, $(\tilde{\sigma})$ is the Stefan−Boltzmann constant and $(\dot{k})$ is the mean absorption coefficient.

Expanding T^4 by using the "Taylor series" and avoiding the higher order terms yields (Eq. (13)).

$$T^4 \cong 4T_\infty^3 T - 3T_\infty^4, \tag{13}$$

In view of Eqs. (12) and (13), Eq. (7) reduces to Eq. (14)

$$\left.\begin{aligned} \mathrm{w}_1\frac{\partial \mathrm{T}}{\partial \mathrm{x}_1}+\mathrm{v}_1\frac{\partial \mathrm{T}}{\partial \mathrm{y}_1}+\frac{\varsigma_o \mathrm{T}}{\widehat{\rho}}\frac{\partial \mathrm{M}^*}{\partial \mathrm{T}}\left(\mathrm{w}\frac{\partial \widehat{\boldsymbol{H}}_1}{\partial \mathrm{x}_1}+v_1\frac{\partial \widehat{\boldsymbol{H}}_1}{\partial \mathrm{y}_1}\right)=\alpha^*\frac{\partial^2 \mathrm{T}}{\partial \mathrm{y}_1^2}-\frac{16\sigma_2 T_\infty^3}{3\mathrm{K}^*\left(\widehat{\rho}C_p\right)_f}\frac{\partial \mathrm{T}}{\partial \mathrm{y}_1}+ \\ \frac{Q_m}{\left(\widehat{\rho}C_p\right)_f}+\tau_1^*\left(\widehat{\mathrm{D}}_B\frac{\partial \mathrm{C}}{\partial \mathrm{y}_1}\frac{\partial \mathrm{T}}{\partial \mathrm{y}_1}+\frac{\widehat{\mathrm{D}}_\mathrm{T}}{T_\infty}\left(\frac{\partial \mathrm{T}}{\partial \mathrm{y}_1}\right)^2\right)+\frac{\widehat{\mu}}{\left(\widehat{\rho}C_p\right)_f}\left(\frac{\partial \mathrm{w}_1}{\partial \mathrm{y}_1}\right)^2, \end{aligned}\right\} \tag{14}$$

2.1. Magnetic dipole

The features of magnetic field influence the ferrofluid flow due to a magnetic dipole. Such impacts of magnetic dipole is pronounced by a magnetic scalar potential $(\boldsymbol{\Omega}_1)$, which is demonstrated as (Eq. (15)).

$$\boldsymbol{\Omega}_1 = \frac{\gamma_1}{2\pi}\frac{x_1}{\left[x_1^2+(y_1+b)^2\right]}, \tag{15}$$

Here (γ_1) represents strength of magnetic field at the source.

The components of magnetic field $(\widehat{\boldsymbol{H}}_1)$ are presented in Eqs. (16) and (17).

$$\frac{\partial \widehat{\boldsymbol{H}}_1}{\partial x_1} = -\frac{\partial \boldsymbol{\Omega}_1}{\partial x_1} = \frac{\gamma_1}{2\pi}\frac{x_1^2-(y_1+b)^2}{\left[x_1^2+(y+b)^2\right]^2}, \tag{16}$$

$$\frac{\partial \widehat{\boldsymbol{H}}_1}{\partial y_1} = -\frac{\partial \boldsymbol{\Omega}_1}{\partial y_1} = \frac{\gamma_1}{2\pi}\frac{2x_1(y_1+b)}{\left[x_1^2+(y_1+b)^2\right]^2}, \tag{17}$$

Since the magnetic body force is normally proportional to the gradient of $(\widehat{\boldsymbol{H}}_1)$, Thus we have (Eq. (18))

$$\widehat{\boldsymbol{H}}_1 = \sqrt{\left(\frac{\partial \boldsymbol{\Omega}_1}{\partial x_1}\right)^2+\left(\frac{\partial \boldsymbol{\Omega}_1}{\partial y_1}\right)^2}, \tag{18}$$

By introducing Eqs. (16) and (17) in Eq. (18), we arrived at Eqs. (19) and (20), after expanded in powers of x_1 and retained terms up to the order of x_1^2

https://doi.org/10.1016/j.heliyon.2019.e01465

$$\frac{\partial \widehat{\boldsymbol{H}}_1}{\partial x_1} = -\frac{\gamma_1}{2\pi}\frac{2x_1}{(y_1+b)^4}, \tag{19}$$

$$\frac{\partial \widehat{\boldsymbol{H}}_1}{\partial y_1} = \frac{\gamma_1}{2\pi}\left[-\frac{2}{(y_1+b)^3}+\frac{4x_1^2}{(y_1+b)^5}\right], \tag{20}$$

The linear form of magnetization (M^*) through temperature T can be approximated by Eq. (21).

$$M^* = \widehat{K}_1(T-T_\infty), \tag{21}$$

Here, $\widehat{K}_1$ identifies as pyromagnetic coefficient. The physical schematic of a heated ferrofluid is shown in Fig. (1). Here the circular lines designate the magnetic field.

We introduce the following dimensionless variables [23].

$$\left.\begin{aligned} &w_1 = d_2 x_1 \mathsf{F}'(\eta_1),\ v_1 = -\sqrt{\frac{d_2\widehat{\mu}}{\widehat{\rho}}}F(\eta_1), \Psi_1 = \frac{\widehat{\mu}\xi_1 \mathsf{F}(\eta_1)}{\widehat{\rho}},\\ &\xi_1 = \sqrt{\frac{d_2\widehat{\mu}}{\widehat{\rho}}}x_1, \Theta(\xi_1,\eta_1) = \frac{T_\infty - T}{T_o - T_w} = \Theta_1(\eta_1)+\xi_1^2\Theta_2(\eta_1),\\ &\eta_1 = \sqrt{\frac{d_2\widehat{\mu}}{\widehat{\rho}}}\mathrm{y}_1, \Phi(\xi_1,\eta_1) = \frac{\mathrm{C}_\infty - \mathrm{C}}{\mathrm{C}_o - \mathrm{C}_w} = \Phi_1(\eta_1)+\xi_1^2\Phi_2(\eta_1), \end{aligned}\right\} \tag{22}$$

Law of conservation of mass (Eq. (4)) is automatically satisfied and flow expressions (Eqs. (6), (7, (8)) are transformed into Eqs. (23), (24), (25), (26), (27).

$$\mathsf{F}''' + \mathsf{F}\mathsf{F}'' - \mathsf{F}'^2 + \widehat{M}_a\left(\mathsf{F}'''\mathsf{F}^2 - 2\mathsf{F}\mathsf{F}'\mathsf{F}''\right) - \frac{2\widehat{\beta}_2\Theta_1}{(\eta_1+\alpha_1)^4} = 0, \tag{23}$$

$$\left.\begin{aligned} &\left(1+N_1^*\right)\Theta_1'' + Pr\left(\mathsf{F}\Theta_1' - 2\mathsf{F}'\Theta_1\right) + \left(\widehat{B}_1\mathsf{F}' + \widehat{B}_2\Theta_1\right) + \frac{2\widehat{\beta}_2\lambda_1\mathsf{F}(\Theta_1-\varepsilon_1)}{(\eta_1+\alpha_1)^3}\\ &+\mathrm{Pr}\widehat{\mathrm{N}}_\mathrm{b}\left(\Theta_1'\Phi_1' + \frac{\widehat{\mathrm{N}}_\mathrm{t}}{\widehat{\mathrm{N}}_\mathrm{b}}\Theta_1'^2\right) - Pr\widehat{S}_1\mathsf{F}' - 4\lambda_1\mathsf{F}'^2 = 0, \end{aligned}\right\} \tag{24}$$

$$\left.\begin{aligned} &\left(1+N_1^*\right)\Theta_2'' - Pr\left(4\mathsf{F}'\Theta_2 - \mathsf{F}\Theta_2'\right) + \widehat{B}_2\Theta_2 + Pr\widehat{\mathrm{N}}_\mathrm{b}\left(\Theta_2'\Phi_1' + \Theta_1'\Phi_2'\right) - \lambda_1\mathsf{F}''^2\\ &+2Pr\widehat{\mathrm{N}}_\mathrm{t}\Theta_1'\Theta_2' + \frac{2\widehat{\beta}_2\lambda_1\mathsf{F}\Theta_2}{(\eta_1+\alpha_1)^3} - \widehat{\beta}_2\lambda_1(\Theta_1-\varepsilon_1)\left(\frac{2\mathsf{F}'}{(\eta_1+\alpha_1)^4}+\frac{4\mathsf{F}}{(\eta_1+\alpha_1)^5}\right), \end{aligned}\right\} \tag{25}$$

https://doi.org/10.1016/j.heliyon.2019.e01465

$$\Phi_1'' + \frac{\widehat{\mathrm{N}}_\mathrm{t}}{\widehat{\mathrm{N}}_\mathrm{b}}\Theta_1'' - PrLe^*\mathsf{F}'\Phi_1 + Sc\mathsf{F}\Phi_1' - PrLe^*\widehat{S}_2\mathsf{F}' - \gamma_2 Sc\Phi_1 = 0, \tag{26}$$

$$\Phi_2'' + \frac{\widehat{\mathrm{N}}_\mathrm{t}}{\widehat{\mathrm{N}}_\mathrm{b}}\Theta_2'' - 3PrLe^*\mathsf{F}'\Phi_2 + Sc\mathsf{F}\Phi_2' - \gamma_2 Sc\Phi_2 = 0, \tag{27}$$

The corresponding boundary conditions (Eq. (28)) will take the form

$$\left.\begin{array}{llll} \mathsf{F}'(0) = 1, & \mathsf{F}(0) = V_s, & \Theta_1(0) = 1 - \widehat{S}_1, & \Theta_2(0) = 0, \\ \Phi_1(0) = 1 - \widehat{S}_2, & \Phi_2(0) = 0, & \mathsf{F}'(\infty) \to 0, & \Theta_1(\infty) \to 0, \\ \Theta_2(\infty) \to 0, & \Phi_1(\infty) \to 0, & \Phi_2(\infty) \to 0, & \end{array}\right\} \tag{28}$$

Mathematically, the non-dimensional governing parameters are defined and are listed below

$\widehat{\beta}_2 = \frac{\gamma_1}{2\pi}\frac{\varsigma_o \widehat{K}_1 \widehat{\rho}(T_o - T_w)}{\widehat{\mu}^2}$	ferrohydrodynamic parameter
$\lambda_1 = \frac{d_2\widehat{\mu}^2}{\widehat{\rho}k^*(T_o - T_w)}$	viscous dissipation
$\widehat{\mathrm{N}}_\mathrm{b} = \frac{\tau_1^*\widehat{D}_B(C_w - C_o)}{\nu}$	Brownion motion parameter
$\widehat{\mathrm{N}}_\mathrm{t} = \frac{\tau_1^*\widehat{D}_T(T_w - T_o)}{\nu T_\infty}$	Thermophoresis parameter
$\alpha_1 = \sqrt{\frac{d_2\widehat{\rho}b^2}{\widehat{\mu}}}$	dimensionless distance
$N_1^* = \frac{16\tilde{\sigma}T_c^3}{3\dot{k}k^*}$	thermal radiation parameter
$\varepsilon_1 = \frac{T_c}{T_o - T_w}$	dimensionless temperature
$\widehat{M}_a = \Gamma_1 d_2$	elastic parameter
$Le^* = \frac{\alpha^*}{\widehat{D}_B}$	Lewis number
$\gamma_2 = \frac{K_2}{d_2}$	chemical reaction parameter,
$\widehat{S}_1 = \frac{\widehat{e}_2}{\widehat{e}_1}$	thermal stratification parameter
$\widehat{S}_2 = \frac{\widehat{e}_4}{\widehat{e}_3}$	Solutal stratification parameter
$Sc = \frac{\nu}{\widehat{D}_B}$	Schmidt number
$Pr = \frac{\widehat{\mu}C_p}{k^*}$	Prandtl number

https://doi.org/10.1016/j.heliyon.2019.e01465

Physical quantities of interest, local Nusselt number and Sherwood number are presented mathematically in Eq. (29)

$$\left.\begin{aligned} Nu_x(Re_x)^{-\frac{1}{2}} &= \frac{x_1 q_w}{k^*(T_o - T_w)} \\ Sh_x(Re_x)^{-\frac{1}{2}} &= \frac{x_1 j_w}{\widehat{D}_B(C_o - C_w)} \end{aligned}\right\}, \tag{29}$$

Where, wall heat and mass fluxes are demarcated in Eq. (30)

$$q_w = -\left|k^*\frac{\partial T}{\partial y_1} + (\widehat{q}_r)_w\right|_{y_1=0}, \quad j_w = -\left|\widehat{D}_B\frac{\partial C}{\partial y_1}\right|_{y_1=0}, \tag{30}$$

Eq. (31) is achieved by substituting Eq. (30) into Eq. (29).

$$\left.\begin{aligned} Nu_x(Re_x)^{-\frac{1}{2}} &= -\left(1 + N_1^*\right)\left[\Theta_1'(0) + \xi_1^2\Theta_2(0)\right] \\ Sh_x(Re_x)^{-\frac{1}{2}} &= -\left[\Phi_1'(0) + \xi_1^2\Phi_2(0)\right] \end{aligned}\right\}, \tag{31}$$

where the local Reynolds number is defined in Eq. (32)

$$Re_x = \frac{\widehat{\rho} c_2 x_1^2}{\widehat{\mu}}. \tag{32}$$

3. Methodology

The numerical code bvp4c [37] in Matlab is developed which uses a collocation method with fourth order accuracy namely finite difference Lobatto IIIA formula. The nonlinear ordinary differential Eqs. (23), (24), (25), (26), (27) subject to the boundary conditions as mentioned in Eq. (28) are cracked through bvp4c Matlab package to attain the numerical results. The error control and mesh selection is created on the residual of the continuous solution. The relative error tolerance has been set to 10^{-6}. The accuracy of our numerical results is declared by comparing them with the analytical results found by the HAM [38] technique for particular cases (see Fig. 21). A comparison given in this figure displays an excellent agreement between these results and gives us confidence in our numerical computations.

The main steps of this numerical technique are as follows:

I. Firstly, we convert the boundary value problem into initial value problem through the substitutions Eqs. (33), (34), (35), (36), (37)

https://doi.org/10.1016/j.heliyon.2019.e01465

$$F = Y_1, \quad F' = Y_1' = Y_2, \quad F'' = Y_2' = Y_3, \tag{33}$$

$$\Theta_1 = Y_4, \quad \Theta_1' = Y_4' = Y_5, \tag{34}$$

$$\Theta_2 = Y_6, \quad \Theta_2' = Y_6' = Y_7, \tag{35}$$

$$\Phi_1 = Y_8, \quad \Phi_1' = Y_8' = Y_9\,, \tag{36}$$

$$\Phi_2 = Y_{10}, \quad \Phi_2' = Y_{10}' = Y_{11}, \tag{37}$$

The flow Eqs. (23), (24), (25), (26), (27)along with boundary conditions (Eq. (28)) are transformed into Eqs. (38), (39), (40), (41), (42), (43)

$$\mathrm{F}''' = YY_1 = \frac{1}{\left(1+\widehat{M}_a Y_1^2\right)}\left[Y_2^2 - Y_1 Y_3 + 2\widehat{M}_a Y_1 Y_2 Y_3 + \frac{2\widehat{\beta}_2 Y_4}{(\eta_1+\alpha_1)^4}\right] \tag{38}$$

$$\Theta_1'' = YY_2 = \frac{1}{\left(1+N_1^*\right)}\left[\begin{array}{l} Pr(2Y_2Y_4 - \mathrm{Y}_1\mathrm{Y}_5) - \left(\widehat{B}_1\mathrm{Y}_2 + \widehat{B}_2\mathrm{Y}_4\right) - \dfrac{2\widehat{\beta}_2\lambda_1 Y_1(Y_4-\varepsilon_1)}{(\eta_1+\alpha_1)^3} \\ -\mathrm{Pr}\widehat{\mathrm{N}}_\mathrm{b}\left(\mathrm{Y}_5\Phi_1' + \dfrac{\widehat{\mathrm{N}}_\mathrm{t}}{\widehat{\mathrm{N}}_\mathrm{b}}Y_5^2\right) + Pr\widehat{S}_1\mathrm{Y}_2 + 4\lambda_1 Y_2^2 \end{array}\right], \tag{39}$$

$$\Theta_2'' = YY_3 = \frac{1}{\left(1+N_1^*\right)}\left[\begin{array}{l} Pr\left(4\mathrm{Y}_2\mathrm{Y}_6 - \mathrm{Y}_1 Y_7^2\right) - Pr\widehat{\mathrm{N}}_\mathrm{b}(\mathrm{Y}_7\mathrm{Y}_9 + \mathrm{Y}_5\mathrm{Y}_{11}) + \lambda_1 Y_3^2 - 2Pr\widehat{\mathrm{N}}_\mathrm{t}\mathrm{Y}_5\mathrm{Y}_7 \\ -\widehat{B}_2\mathrm{Y}_6 - \dfrac{2\widehat{\beta}_2\lambda_1 Y_1\mathrm{Y}_6}{(\eta_1+\alpha_1)^3} + \widehat{\beta}_2\lambda_1(\mathrm{Y}_5-\varepsilon_1)\left(\dfrac{2\mathrm{Y}_2}{(\eta_1+\alpha_1)^4} + \dfrac{4\mathrm{Y}_1}{(\eta_1+\alpha_1)^5}\right) \end{array}\right], \tag{40}$$

$$\Phi_1'' = YY_4 = PrLe^*\mathrm{Y}_2\mathrm{Y}_8 - \frac{\widehat{\mathrm{N}}_\mathrm{t}}{\widehat{\mathrm{N}}_\mathrm{b}}YY_2 - Sc\mathrm{Y}_1\mathrm{Y}_9 + PrLe^*\widehat{S}_2\mathrm{Y}_2 + \gamma_2 ScY_8, \tag{41}$$

$$\Phi_2'' = YY_5 = 3PrLe^*\mathrm{Y}_2\mathrm{Y}_{10} - \frac{\widehat{\mathrm{N}}_\mathrm{t}}{\widehat{\mathrm{N}}_\mathrm{b}}YY_3 - Sc\mathrm{Y}_1\mathrm{Y}_{11} + \gamma_2 ScY_{10}, \tag{42}$$

with the allied boundary conditions

https://doi.org/10.1016/j.heliyon.2019.e01465

$$\left.\begin{array}{lll} Y_1(0)=0, & Y_2(0)=1, & Y_2(\infty)=0, \\ Y_4(0)=1-\widehat{S}_1, & & Y_4(\infty)=0, \\ Y_6(0)=0, & & Y_6(\infty)=0, \\ Y_8(0)=1-\widehat{S}_2, & & Y_8(\infty)=0, \\ Y_{10}(0)=0, & & Y_{10}(\infty)=0. \end{array}\right\} \tag{43}$$

4. Results and discussion

Numerical solutions of resulting nonlinear differential equations $(38-42)$ subjected to boundary conditions (Eq. (43)) are obtained by using the Matlab routine bvp4c that uses Collocation method. Further the behavior of sundry flow variables on velocity $(\mathrm{F}'(\eta_1))$, temperature $(\Theta_1(\eta_1),\Theta_2(\eta_1))$, skin fraction (C_F), Nusselt number (Nu_x), concentration $(\Phi_1(\eta_1),\Phi_2(\eta_1))$ and Sherwood number (Sh_x) are delibrated through Figs. 2, 3, 4, 5, 6, 7, 8, 9, 10, 11, 12, 13, 14, 15, 16, 17, 18, 19, 20, 21, 22, 23, 24, and 25. Table 1 conveys the computational results of Nusselt number against certain physical factors. Here heat transfer rate enhances for greater $(\widehat{\mathrm{N}}_\mathrm{t})$, $(\widehat{\beta}_2)$, $(\widehat{M}_a)$ and (Sc) while it diminishes for (ε_1), (λ_1), $(\widehat{\mathrm{N}}_\mathrm{b})$ and (α_1). Table 2 provides numerical values of Sherwood number for different physical parameters. This table shows that mass transfer rate increases for higher estimation of (α_1), $(\widehat{\beta}_2)$ and (Pr), and declines with an increase in the values of (λ_1) and $(\widehat{\mathrm{N}}_\mathrm{t})$. Figs. 2, 3, 4, and 5 are publicized to check the behaviour of $(\widehat{\beta}_2)$, $(\widehat{S}_1)$, $(\widehat{M}_a)$ and (V_s) on velocity $\mathrm{F}'(\eta_1)$. Fig. 2 shows the declining trend of $\mathrm{F}'(\eta_1)$ for higher estimation of ferromagnetic parameter $(\widehat{\beta}_2)$. Physically higher values of $(\widehat{\beta}_2 = 0.1, 0.5, 1.0, 1.5)$ develops more resistance to the fluid flow. That ultimately declines the velocity $\mathrm{F}'(\eta_1)$profile. The effects of $(\widehat{S}_1)$ on $\mathrm{F}'(\eta_1)$ are evident in Fig. 3. For greater estimation of $(\widehat{S}_1 = 0.1, 1.0, 2.0, 3.0)$, velocity $\mathrm{F}'(\eta_1)$ curve and related boundary layer thickness decreases. Since density of fluid layers becomes thicker in vertical

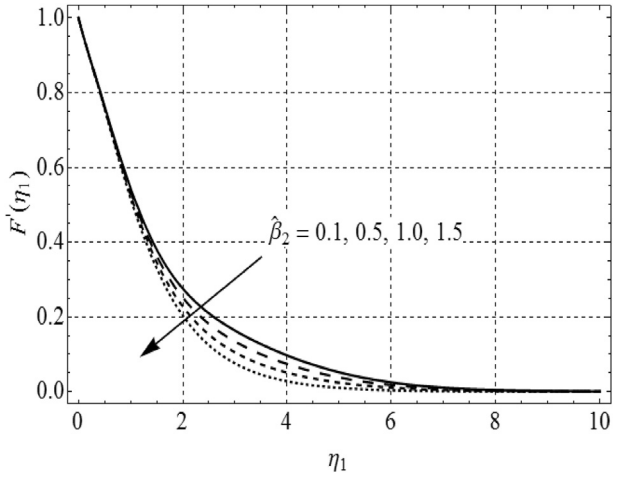

Fig. 2. $\mathrm{F}'(\eta_1)$ *against* $\widehat{\beta}_2$.

https://doi.org/10.1016/j.heliyon.2019.e01465

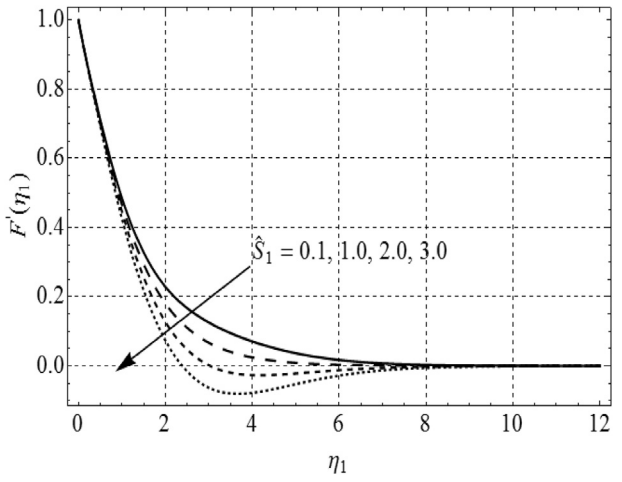

Fig. 3. $\mathrm{F}'(\eta_1)$ *against* $\widehat{S}_1$.

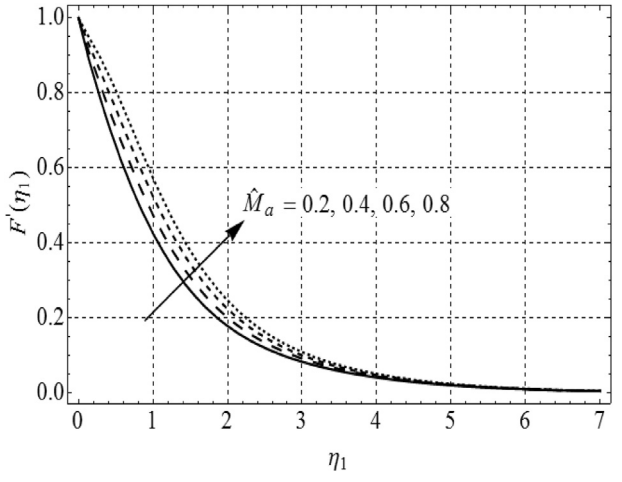

Fig. 4. $\mathrm{F}'(\eta_1)$ *against* $\widehat{M}_a$.

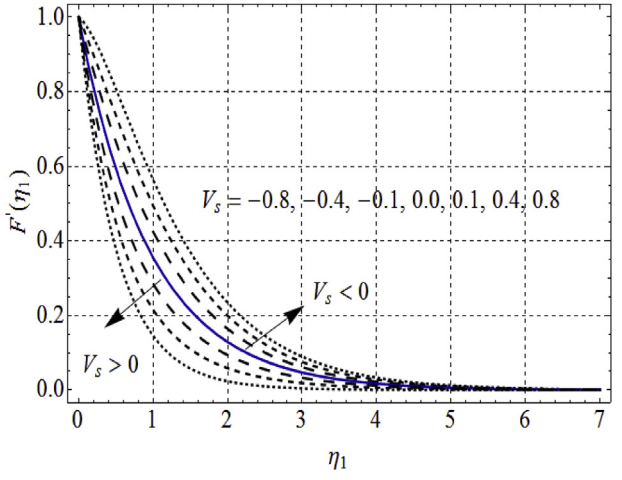

Fig. 5. $\mathrm{F}'(\eta_1)$ *against* V_s.

https://doi.org/10.1016/j.heliyon.2019.e01465

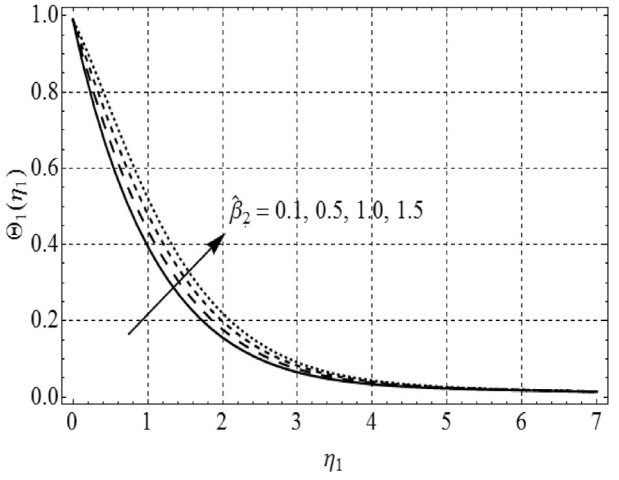

Fig. 6. $\Theta_1(\eta_1)$ *against* $\widehat{\beta}_2$.

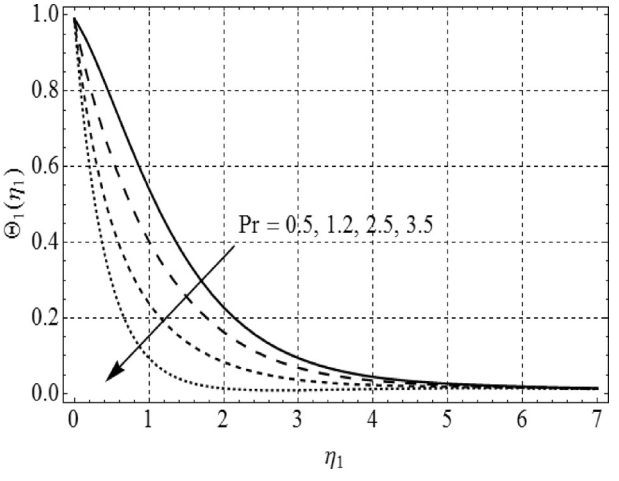

Fig. 7. $\Theta_1(\eta_1)$ *against* Pr.

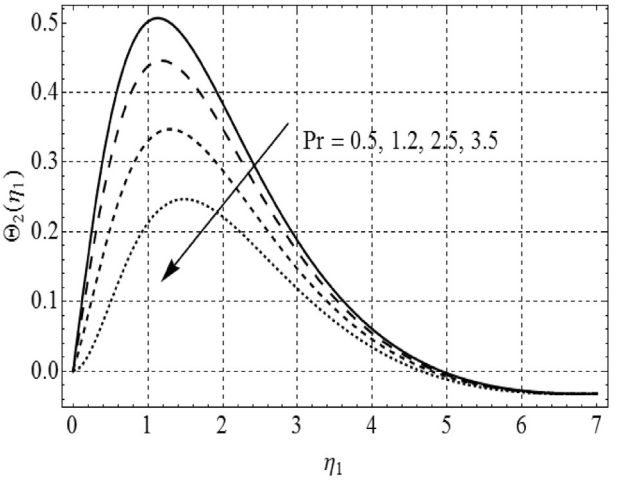

Fig. 8. $\Theta_2(\eta_1)$ *against* Pr.

https://doi.org/10.1016/j.heliyon.2019.e01465

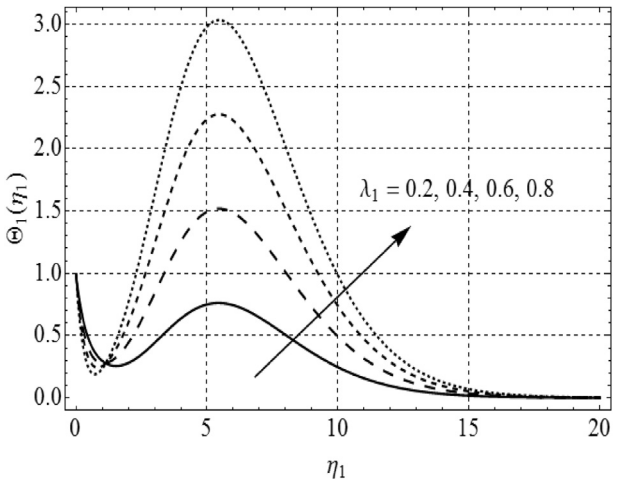

Fig. 9. $\Theta_1(\eta_1)$ *against* λ_1.

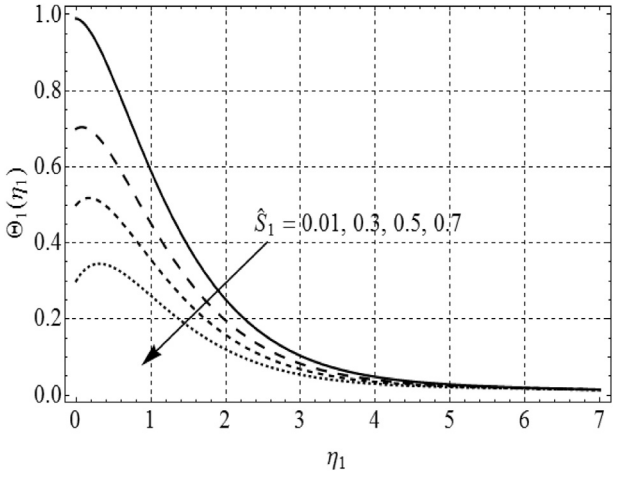

Fig. 10. $\Theta_1(\eta_1)$ *against* $\widehat{S}_1$.

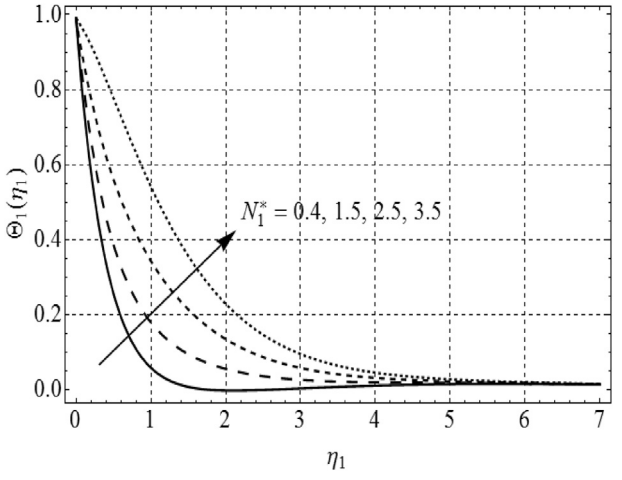

Fig. 11. $\Theta_1(\eta_1)$ *against* N_1^*.

https://doi.org/10.1016/j.heliyon.2019.e01465

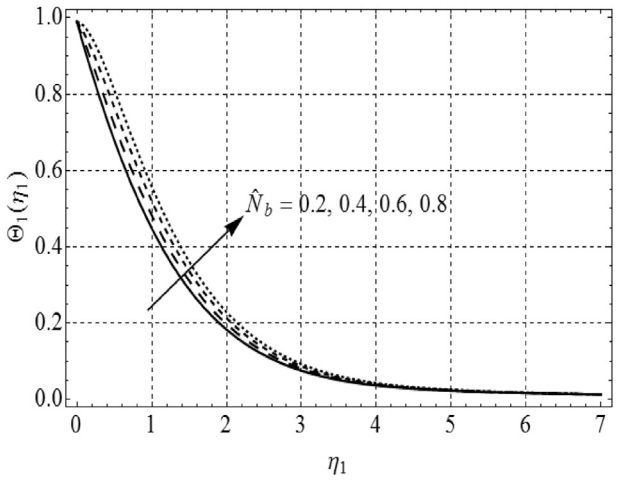

Fig. 12. $\Theta_1(\eta_1)$ *against* $\widehat{N}_b$.

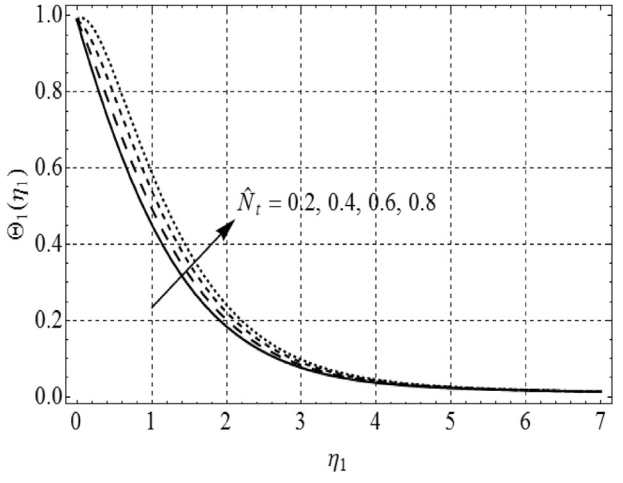

Fig. 13. $\Theta_1(\eta_1)$ *against* $\widehat{N}_t$.

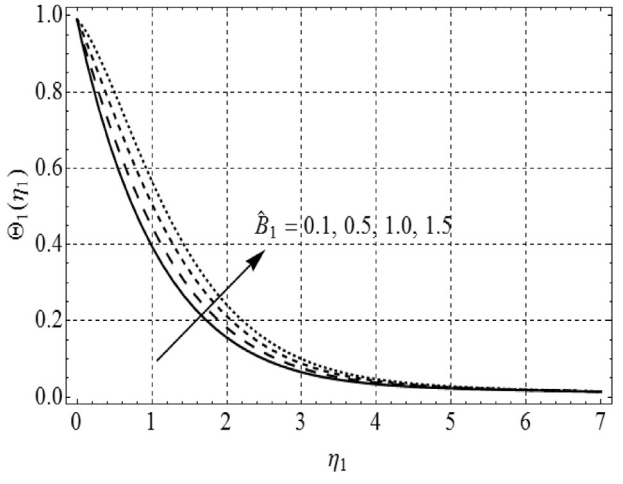

Fig. 14. $\Theta_1(\eta_1)$ *against* $\widehat{B}_1$.

https://doi.org/10.1016/j.heliyon.2019.e01465

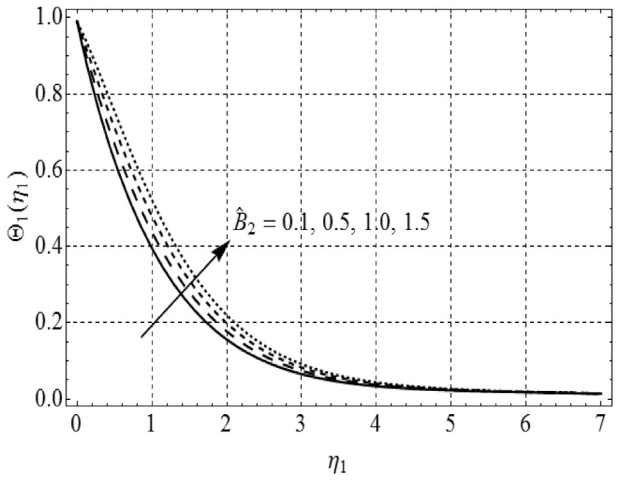

Fig. 15. $\Theta_1(\eta_1)$ *against* $\widehat{B}_2$.

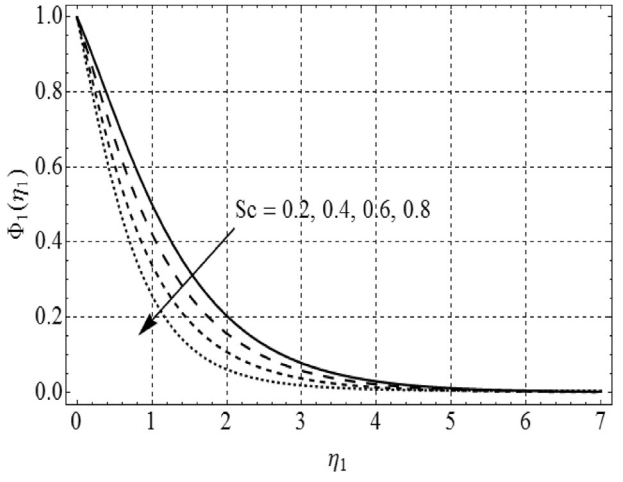

Fig. 16. $\Phi_1(\eta_1)$ *against Sc*.

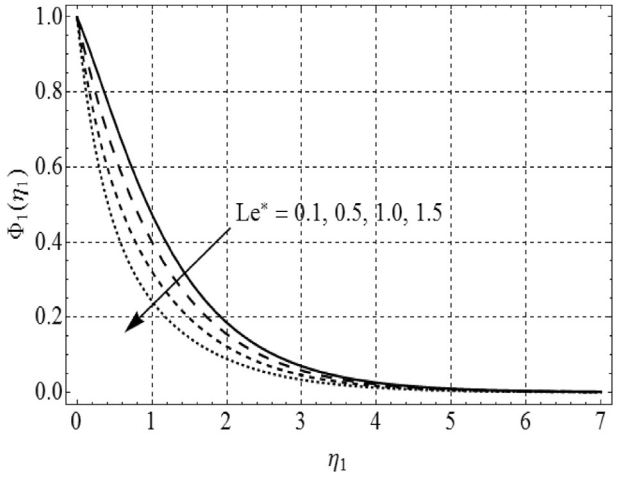

Fig. 17. $\Phi_1(\eta_1)$ *against* Le^*.

https://doi.org/10.1016/j.heliyon.2019.e01465

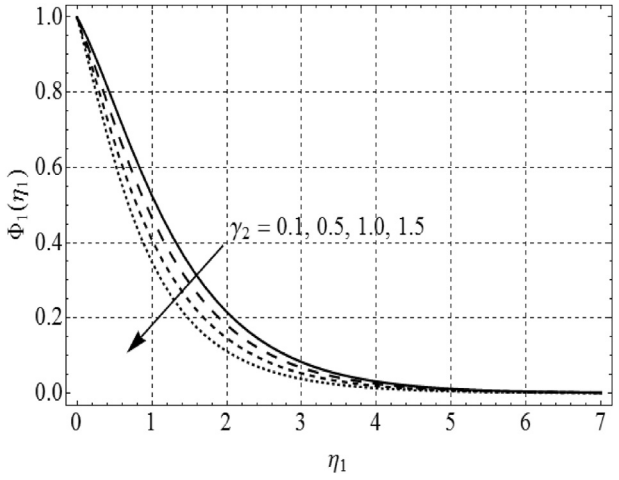

Fig. 18. $\Phi_1(\eta_1)$ *against* γ_2.

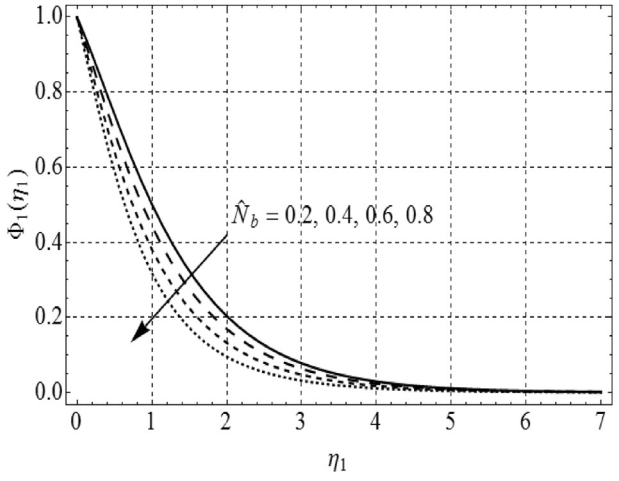

Fig. 19. $\Phi_1(\eta_1)$ *against* $\widehat{N}_b$.

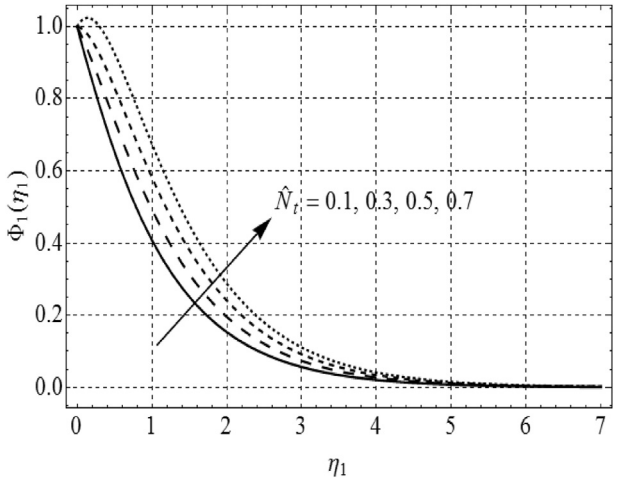

Fig. 20. $\Phi_1(\eta_1)$ *against* $\widehat{N}_t$.

https://doi.org/10.1016/j.heliyon.2019.e01465

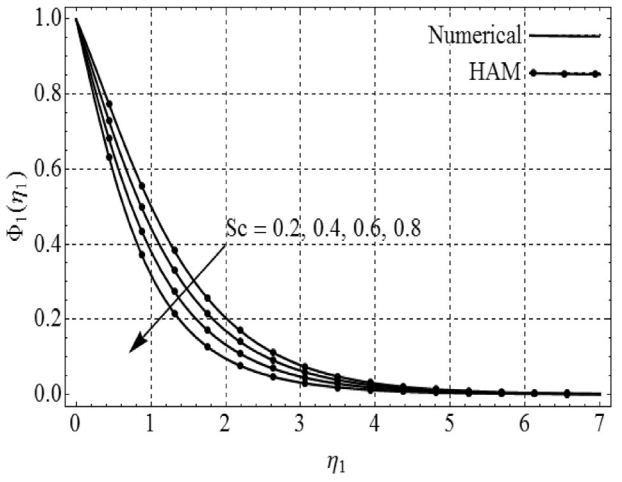

Fig. 21. Comparison of numerical and analytical results.

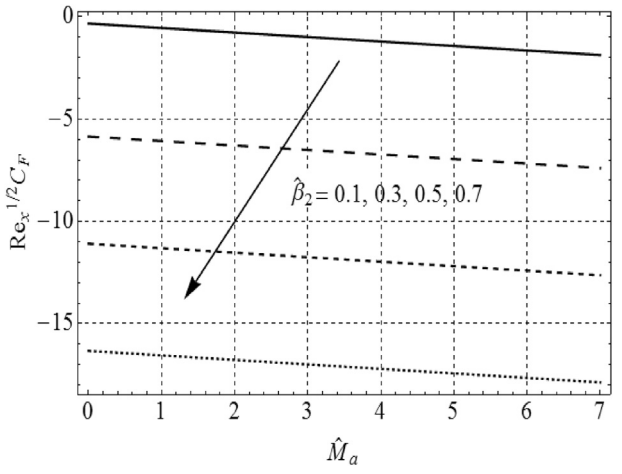

Fig. 22. $C_F(Re_x)^{1/2}$ *against* $\widehat{\beta}_2$.

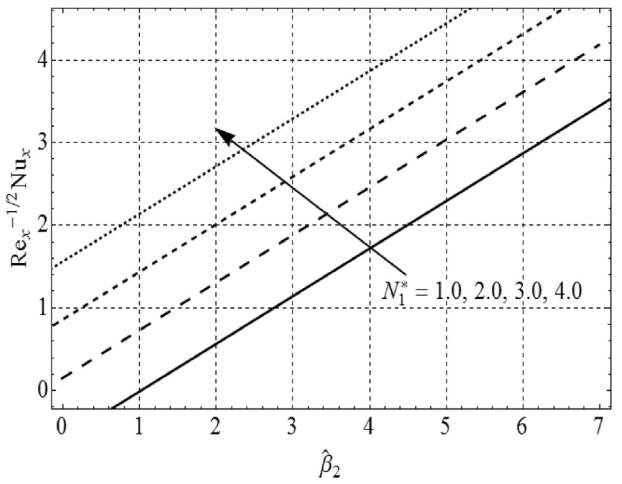

Fig. 23. $Nu_x(Re_x)^{-1/2}$ *against* N_1^*.

https://doi.org/10.1016/j.heliyon.2019.e01465

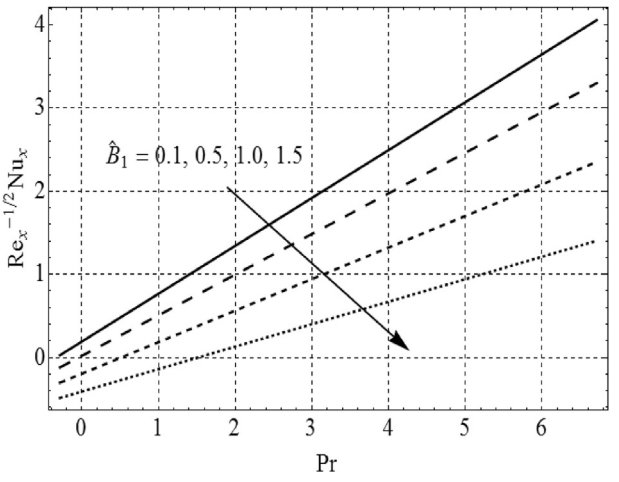

Fig. 24. $Nu_x(Re_x)^{-½}$ *against* $\widehat{B}_1$.

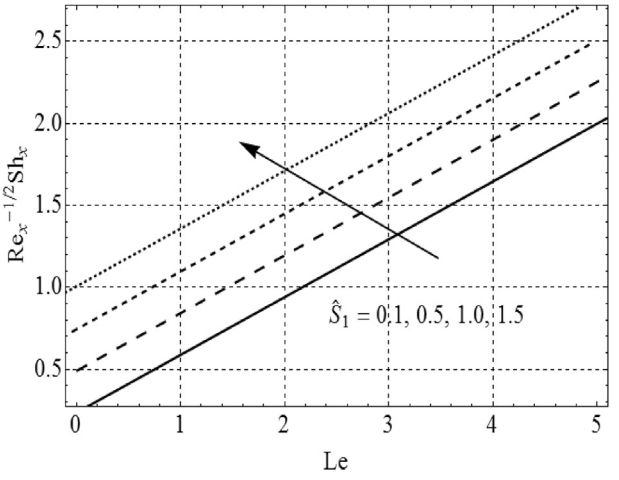

Fig. 25. $Sh_x(Re_x)^{-½}$ *against* $\widehat{S}_1$.

direction for greater values of thermal stratification parameter $(\widehat{S}_1)$. Due to this fact, magneto-hydrodynamic interaction rises and consequently $F'(\eta_1)$reduces. Increasing trend of elasticity parameter $(\widehat{M}_a = 0.1,\ 0.5,\ 1.0,\ 1.5)$ on velocity $F'(\eta_1)$distribution is deliberated in Fig. 4. It is declared that for growing values of parameter $(\widehat{M}_a)$ velocity profile enhances gradually, the result specifies that velocity profile and corresponding boundary layer turns to be thicker with an increase of $(\widehat{M}_a)$. It is inspected that response velocity boost up with increases of an elastic force of the working fluid. When $\widehat{M}_a = 0$, the surface forces reach its minimum level, which shows the absence of the internal elastic force of fluid, due to which the non-Newtonian fluid transform into a Newtonian liquid. Fig. 5 elucidates the influence of the permeability parameter (V_s)on the fluid velocity profile $F'(\eta_1)$. The

https://doi.org/10.1016/j.heliyon.2019.e01465

Table 1. Variation of $Nu_x(Re_x)^{-\frac{1}{2}}$ for different parameters.

$\widehat{\beta}_2$	N_1^*	λ_1	$\widehat{N}_b$	$\widehat{B}_1$	α_1	ε_1	Sc.	$\widehat{M}_a$	$\widehat{N}_t$	Pr.	$Nu_x(Re_x)^{-\frac{1}{2}}$
0.2	0.4	0.3	0.2	0.3	0.2	0.1	0.3	0.5	0.3	1.2	**0.75462**
0.4											0.71645
0.6											0.65743
	0.4										**0.75462**
	0.6										0.70644
	0.8										0.66932
		0.1									0.78457
		0.3									**0.75462**
		0.5									0.67240
			0.2								**0.75462**
			0.3								0.77046
			0.4								0.81541
				0.1							0.75831
				0.3							**0.75462**
				0.5							0.75262
					0.2						**0.75462**
					0.4						0.76524
					0.6						0.77035
						0.1					**0.75462**
						0.2					0.75758
						0.3					0.75956
							0.3				**0.75462**
							0.5				0.75263
							0.7				0.75125
								0.1			0.75489
								0.5			**0.75462**
								1.0			0.75437
									0.1		0.74658
									0.3		**0.75462**
									0.5		0.76454
										0.5	0.58485
										1.0	0.65274
										1.2	**0.75462**

https://doi.org/10.1016/j.heliyon.2019.e01465

Table 2. Variation of $Sh_x(Re_x)^{-\frac{1}{2}}$ for different parameters.

$\widehat{\beta}_2$	N_1^*	λ_1	$\widehat{N}_b$	$\widehat{B}_1$	α_1	ε_1	Sc.	$\widehat{M}_a$	$\widehat{N}_t$	Pr.	$-\mathrm{S}h_x(\mathrm{R}e_x)^{-\frac{1}{2}}$
0.2	0.4	0.4	0.2	0.3	0.2	0.1	0.3	0.5	0.3	1.2	**0.56862**
0.4											0.56629
0.6											0.56417
	0.4										**0.56862**
	0.6										0.58473
	0.8										0.62764
		0.2									0.56713
		0.4									**0.56862**
		0.6									0.56936
			0.2								**0.56862**
			0.3								0.56941
			0.4								0.57254
				0.1							0.56643
				0.3							**0.56862**
				0.5							0.56956
					0.2						**0.56862**
					0.4						0.56852
					0.6						0.56846
						0.1					**0.56862**
						0.2					0.56733
						0.3					0.56706
							0.3				**0.56862**
							0.5				0.56786
							0.7				0.56824
								0.1			0.52357
								0.5			**0.56862**
								1.0			0.63484
									0.1		0.58476
									0.2		**0.56862**
									0.3		0.54591
										0.5	0.52328
										1.0	0.54752
										1.2	**0.56862**

https://doi.org/10.1016/j.heliyon.2019.e01465

graphical facts represent that boundary layer thickness declines for suction case while injection is in opposite trend.

Figs. 6, 7, 8, 9, 10, 11, 12, 13, 14, and 15 are portrayed to investigate the impact of $(\widehat{\beta}_2)$, (Pr), (λ_1), $(\widehat{S}_1)$, (N_1^*), $(\widehat{N}_b)$, $(\widehat{N}_t)$, $(\widehat{B}_1)$ and $(\widehat{B}_2)$ on temperature $\Theta_1(\eta_1)$. Fig. 6 is portrayed to study the feature of $(\widehat{\beta}_2)$ on temperature $\Theta_1(\eta_1)$. It is noticed that temperature $\Theta_1(\eta_1)$ is an increasing function of $(\widehat{\beta}_2 = 0.1, 0.5, 1.0, 1.5)$. It is due to the interaction between motion of fluid particles and an action of a magnetic field. This interaction between fluid particles and magnetic field action diminishes velocity field thereby ascending frictional heating amid fluid layers leads to be thicken thermal boundary layer. Thus, reduction in movements of fluid particles leads to an enhancement in heat transfer (see Fig. 6). Variation of $(Pr = 0.5, 1.2, 2.5, 3.5)$ on temperature $\Theta_1(\eta_1)$ and $\Theta_2(\eta_1)$ is displayed in Figs. 7 and 8. Similar decreasing nature of both temperature and associated layer thickness is pronounced for greater values of (Pr). Since inverse relation exists between (Pr) and thermal diffusivity. Thus, an increase in Prandtl number (Pr)corresponds to lower the thermal diffusivity of fluid that declines the role of $\Theta_1(\eta_1)$ and $\Theta_2(\eta_1)$. Fig. 9 displays the effect of Eckert number (λ_1) on temperature $\Theta_1(\eta_1)$. For greater values of $(\lambda_1 = 0.2, 0.4, 0.6, 0.8)$ temperature $\Theta_1(\eta_1)$ is found to be heighten near the surface. Since greater (λ_1) produces more kinetic energy, due to which particles collide frequently with each other and they dissipate energy. As a result kinetic energy is converted into the thermal energy that causes a rise in $\Theta_1(\eta_1)$. Feature of thermally stratified parameter $(\widehat{S}_1)$ against $\Theta_1(\eta_1)$ is presented in Fig. 10. Here temperature and thermal boundary layer are reduced for higher $(\widehat{S}_1 = 0.01, 0.3, 0.5, 0.7)$. In fact temperature difference $(T_w - T_\infty)$ gradually decreases for higher values of $(\widehat{S}_1)$ and hence temperature $\Theta_1(\eta_1)$ decreases. Fig. 11 highlights the effect of thermal radiation parameter (N_1^*) on temperature $\Theta_1(\eta_1)$ curve. Since temperature $\Theta_1(\eta_1)$ curve increases as the radiation upsurges. This can be accredited to the physical statistic that the thermal boundary layer thickness intensifies with increasing radiation parameter. Influence of $(\widehat{N}_b = 0.2, 0.4, 0.6, 0.8)$ and $(\widehat{N}_t = 0.1, 0.3, 0.5, 0.7)$ on temperature $\Theta_1(\eta_1)$ is displayed in Figs. 12 and 13. Similar enhancing conduct of both parameters $(\widehat{N}_b)$ and $(\widehat{N}_t)$ are observed for $\Theta_1(\eta_1)$ and related boundary layer thickness. In fact, additional heat is produced through the random motion of fluid particles inside the frame of larger Brownian motion parameter $(\widehat{N}_b)$. Consequently, temperature $\Theta_1(\eta_1)$ distribution increases. For larger $(\widehat{N}_t)$thermophoresis force drives the fluid particles more rapidly from hotter to colder regions in the medium. Therefore $\Theta_1(\eta_1)$ enhances (see Fig. 13). Figs. 14 and 15 are revealed to identify the nature of $\Theta_1(\eta_1)$ for distinct values of heat generation/absorption parameters $(\widehat{B}_1 = 0.1, 0.5, 1.0, 1.5)$ and $(\widehat{B}_2 = 0.1, 0.5, 1.0, 1.5)$. Enhancing nature of $\Theta_1(\eta_1)$ is noticed for both parameters

https://doi.org/10.1016/j.heliyon.2019.e01465

$(\widehat{B}_1)$ and $(\widehat{B}_2)$. Bodily, higher appraisal of $(\widehat{B}_1)$ increases the boundary layer thickness and hence it acts as an agent to generate heat. Due to this reason, an amplification in $\Theta_1(\eta_1)$ is professed for higher $(\widehat{B}_1)$ (see Fig. 13). Figs. 16, 17, 18, 19, and 20 are scrutinized the behavior of concentration $\Phi_1(\eta_1)$ against (Sc), (Le^*), (γ_2) $(\widehat{\mathrm{N}}_\mathrm{b})$and $(\widehat{\mathrm{N}}_\mathrm{t})$ respectively. Behavior of $(\mathrm{Sc} = 0.2,\ 0.4,\ 0.6,\ 0.8)$ on $\Phi_1(\eta_1)$is exposed in Fig. 16. Here $\Phi_1(\eta_1)$is a decreasing function of (Sc). Physically, (Sc) enhances momentum diffusivity and thus concentration $\Phi_1(\eta_1)$curve decreases. Effect of Lewis number $(Le^* = 0.1,\ 0.5,\ 1.0,\ 1.5)$ is sketched to analyze the concentration $\Phi_1(\eta_1)$ in Fig. 17. An increase in Lewis number (Le^*) leads to decrease in $\Phi_1(\eta_1)$. Fig. 18 points out the impact of (γ_2) on $\Phi_1(\eta_1)$. Here $\Phi_1(\eta_1)$ and corresponding layer thickness are reduced for higher estimation of $(\gamma_2 > 0)$. Moreover it is noticed that behavior of destructive chemical reaction $(\gamma_2 > 0)$ is quite reverse when compared with the case of generative chemical reaction $(\gamma_2 < 0)$. Figs. 19 and 20 are designed to study the behavior of concentration $\Phi_1(\eta_1)$ distribution for larger Brownian $(\widehat{\mathrm{N}}_\mathrm{b})$ and thermophoresis $(\widehat{\mathrm{N}}_\mathrm{t})$parameters. It is noticed from Fig. 19 that concentration $\Phi_1(\eta_1)$ profile is reduced with rise in Brownian parameter $(\widehat{\mathrm{N}}_\mathrm{b} = 0.2,\ 0.4,\ 0.6,\ 0.8)$. Physically, $(\widehat{\mathrm{N}}_\mathrm{b})$ rises Brownian diffusion rate and as a result concentration $\Phi_1(\eta_1)$ diminishes. For greater values of $(\widehat{\mathrm{N}}_\mathrm{t} = 0.1,\ 0.3,\ 0.5,\ 0.7)$ concentration $\Phi_1(\eta_1)$ profile upsurges (see Fig. 20). Higher $(\widehat{\mathrm{N}}_\mathrm{t})$ offers the rise in thermal conductivity of the fluid that ultimately produces enhancement in $\Phi_1(\eta_1)$. The accuracy of the obtained numerical results is shown by comparing numerical results with the analytical results computed by means of the homotopy analysis method (HAM) through Fig. 21. This comparison leads to an excellent agreement of the analytical solutions with the numerical ones. Feature of skin friction coefficient (C_F), local Nusselt (Nu_x) and Sherwood (Sh_x) numbers for $(\widehat{\beta}_2)$, $(\widehat{M}_a)$, (N_1^*) , $(\widehat{S}_1)$ and (Le^*) are presented in Figs. 22, 23, 24, and 25. Impact of skin friction coefficient against $(\widehat{M}_a)$ is portrayed in Fig. 22 for higher marks of $(\widehat{\beta}_2 = 0.1,\ 0.3,\ 0.5,\ 0.7)$. Figs. 23 and 24 are presented to investigate Nusselt number (Nu_x) for greater values of $(\mathrm{N}_1^* = 1.0,\ 2.0,\ 3.0, 4.0)$ and $(\widehat{B}_1 = 0.1,\ 0.5,\ 1.0,\ 1.5)$. The Rate of heat transfer $\left(Nu_x(Re_x)^{-\frac{1}{2}}\right)$ enriches for (N_1^*) (see Fig. 22) while it declines for greater marks of $(\widehat{B}_1)$. An enhancing trend of Sherwood $\left(Sh_x(Re_x)^{-\frac{1}{2}}\right)$ is also observed from Fig. 25 for greater $(\widehat{S}_1 = 0.1,\ 0.5,\ 1.0,\ 1.5)$.

5. Conclusions

In this article, the effect of nonlinear thermal radiation on ferromagnetic Maxwell fluid in presence of magnetic dipole is analyzed numerically over a permeable stretching sheet. The key points of the flow problem are summarized as follows:

https://doi.org/10.1016/j.heliyon.2019.e01465

I. Velocity profile $F'(\eta_1)$ declines for ferromagnetic parameter $(\widehat{\beta}_2)$and thermal stratification parameters $(\widehat{S}_1)$, while it has reverse features for elastic parameter $(\widehat{M_a})$.

II. The behavior of temperature distribution and apposite thermal boundary layer thickness could be observed as monotonically increasing for thermal radiation parameter (N_1^*), ferromagnetic parameter $(\widehat{\beta}_2)$ and thermophoresis diffusion coefficient $(\widehat{N}_t)$while it reduces with Prandtl number (Pr) and thermal stratification parameter $(\widehat{S}_1)$.

III. Positive values of heat source/sink parameters $(\widehat{B}_1, \widehat{B}_2)$ act like heat generators and negative values correspond to the heat absorber. Hence space and temperature dependent heat absorption are more appropriate for cooling purposes.

IV. Concentration profile and solutal boundary layer thickness upsurges for greater values of $(\widehat{N}_t)$ and it reduces for higher estimation of (Le^*), (Sc) and $(\widehat{N}_b)$.

V. Concentration field is quite reverse for $\gamma_2 > 0$ and $\gamma_2 < 0$.

VI. An increase in Lewis number (Le^*) is a source of reduction in the concentration distribution and associated boundary layer thickness.

VII. Local Nusselt (Nu_x) and Sherwood (Sh_x) numbers have a reverse effect with thermal radiation parameter (N_1^*), Prandtl number (Pr) and thermophoretic diffusion coefficient $(\widehat{N}_t)$and both quantities declines for ferrohydrodynamic parameter $(\widehat{\beta}_2)$.

Declarations

Author contribution statement

Misbah Ijaz: Conceived and designed the analysis; Analyzed and interpreted the data; Contributed analysis tools or data; Wrote the paper.

Muhammad Ayub: Conceived and designed the analysis; Analyzed and interpreted the data.

Funding statement

This research did not receive any specific grant from funding agencies in the public, commercial, or not-for-profit sectors.

Competing interest statement

The authors declare no conflict of interest.

https://doi.org/10.1016/j.heliyon.2019.e01465

Additional information

The Authors are thankful to the reviewers for their most useful comments and suggestions that significantly improved our paper.

References

[1] A. Pantokratoras, Natural convection along a vertical isothermal plate with linear and nonlinear Rosseland thermal radiation, Int. J. Therm. Sci. 84 (2014) 151−157.

[2] A. Mushtaq, M. Mustafa, T. Hayat, A. Alsaedi, On the numerical solution of the nonlinear radiation heat transfer problem in a three-dimensional flow, Z. Naturforsch. 69 (2014) 705−713.

[3] M.R. Krishnamurthy, B.C. Prasannakumara, B.J. Gireesha, R.S.R. Gorla, Effect of chemical reaction on MHD boundary layer flow and melting heat transfer of Williamson nanofluid in porous medium, Eng. Sci. Technol. Int. J 19 (1) (2016) 53−61.

[4] R. Cortell, Fluid flow and radiative nonlinear heat transfer over a stretching sheet, J. King Saud Univ. Sci. 26 (2014) 161−167.

[5] F. Mabood, S.M. Ibrahim, M.M. Rashidi, M.S. Shadloo, L. Giulio, Non-uniform heat source/sink and Soret effects on MHD nonDarcian convective flow past a stretching sheet in a micropolar fluid with radiation, Int. J. Heat Mass Transf. 93 (2016) 674−682.

[6] M.I. Khan, M. Waqas, T. Hayat, M.I. Khan, A. Alsaedi, Numerical simulation of nonlinear thermal radiation and homogeneous-heterogeneous reactions in convective flow by a variable thicked surface, J. Mol. Liq. 246 (2017) 259−267.

[7] M. Khan, M. Irfan, W.A. Khan, Impact of nonlinear thermal radiation and gyrotactic microorganisms on the Magneto-Burgers nanofluid, Int. J. Mech. Sci. 130 (2017) 375−382.

[8] T. Hayat, S. Qayyum, A. Alsaedi, M. Waqas, Simultaneous influences of mixed convection and nonlinear thermal radiation in stagnation point flow of Oldroyd-B fluid towards an unsteady convectively heated stretched surface, J. Mol. Liq. 224 (2016) 811−817.

[9] T. Hayat, S.A. Shehzad, H.H. Al-Sulami, S. Asghar, Influence of thermal stratification on the radiative flow of Maxwell fluid, J. Braz. Soc. Mech. Sci. Eng. 35 (2013) 381−389.

https://doi.org/10.1016/j.heliyon.2019.e01465

[10] M. Ijaz, M. Ayub, M. Zubair, A. Riaz, On stratified flow of ferromagnetic nanofluid with heat generation/absorption, Phys. Scripta (2018).

[11] W. Ibrahim, O.D. Makinde, The effect of double stratification on boundary layer flow and heat transfer of nanofluid over a vertical plate, Comp Fluids 86 (2013) 433–441.

[12] M. Ijaz, M. Ayub, Nonlinear convective stratified flow of Maxwell nanofluid with activation energy, Heliyon 5 (2019), e01121.

[13] T. Hayat, T. Hussain, S.A. Shehzad, A. Alsaedi, Thermal and concentration stratifications effects in radiative flow of Jeffrey fluid over a stretching sheet, PLoS One (2014).

[14] D. Srinivasacharya, O. Surender, Non-Darcy mixed convection in a doubly stratified porous medium with soret-dufour effects, Int. J. Eng. Maths (2014).

[15] T. Hayat, M. Imtiaz, A. Alsaedi, Unsteady flow of nanofluid with double stratification and magnetohydrodynamics, Int. J. Heat Mass Transf. 92 (2016) 100–109.

[16] H.I. Andersson, O.A. Valnes, Flow of a heated ferrofluid over a stretching sheet in the presence of a magnetic dipole, Acta Mech. 128 (1998) 39–47.

[17] A. Zeeshan, A. Majeed, R. Ellahi, Effect of magnetic dipole on viscous ferrofluid past a stretching surface with thermal radiation, J. Mol. Liq. 215 (2016) 549–554.

[18] M. Zubair, M. Ijaz, T. Abbas, A. Riaz, Analysis of modified Fourier law in flow of ferromagnetic Powell-Eyring fluid considering two equal magnetic dipoles, Can. J. Phys. (2018).

[19] N. Muhammad, S. Nadeem, R.U. Haq, Heat transport phenomenon in the ferromagnetic fluid over a stretching sheet with thermal stratification, Results Phys. 7 (2017) 854–861.

[20] T. Hayat, S. Ahmed, M.I. Khan, A. Alsaedi, Exploring magnetic dipole contribution on radiative flow of ferromagnetic Williamson fluid, Results Phys 8 (2018) 545–551.

[21] J.L. Neuringer, R.E. Rosensweig, Ferrohydrodynamics, Phys. Fluids 7 (1964) 1927–1937.

[22] M. Imtiaz, T. Hayat, A. Alsaedi, Convective flow of ferrofluid due to a curved stretching surface with homogeneous-heterogeneous reactions, Powder Tech 310 (2017) 154–162.

https://doi.org/10.1016/j.heliyon.2019.e01465

[23] H.I. Andersson, O.A. Valnes, Flow of heated ferrofluid over a stretching sheet in the presence of a magnetic dipole, Acta Mech. 128 (1998) 39–47.

[24] L.S.R. Titus, A. Abraham, Heat transfer in Ferrofluid flow over a stretching sheet with radiation, Int. J. Eng. Res. Tech. 3 (2014) (ISSN:2278-0181).

[25] T. Hayat, S. Ahmad, M.I. Khan, A. Alseadi, Non-Darcy Forchheimer flow of ferromagnetic second grade fluid, Res. Phys. 7 (2017) 3419–3424.

[26] A.J. Chamka, A.M. Aly, M.A. Mansour, Similarity solution for unsteady heat and mass transfer from a stretching surface embedded in a porous medium with suction/injection and chemical reaction effects, Chem. Eng. Commun. 197 (2010) 846–858.

[27] D. Pal, H. Mondal, MHD non-Darcy mixed convection heat and mass transfer over a nonlinear stretching sheet with Soret-Dufour effects and chemical reaction, Int. Commun. Heat Mass Transf. 38 (2011) 463–467.

[28] S. Srinivas, P.B.A. Reddy, B.S.R.V. Prasad, Non-Darcian unsteady flow of a micropolar fluid over a porous stretching sheet with thermal radiation and chemical reaction, Heat Transf. Asian Res. (2013). Online First.

[29] N.A. Khan, F. Riaz, F. Sultan, Effects of chemical reaction and magnetic field on a couple stress fluid over a non-linearly stretching sheet, Eur. Phys. J. Plus 129 (2014) 18.

[30] T. Hayat, M.I. Khan, M. Waqas, A. Alsaedi, M. Farooq, Numerical simulation for melting heat transfer and radiation effects in stagnation point flow of carbon-water nanofluid, Comput. Methods Appl. Mech. Eng. 315 (2017) 1011–1024.

[31] T. Hayat, M. Tamoor, M.I. Khan, A. Alsaedi, Numerical simulation for nonlinear radiative flow by convective cylinder, Results Phys 6 (2016) 1031–1035.

[32] T. Hayat, S. Ahmad, M. I Khan, A. Alsaedi, Simulation of ferromagnetic nanomaterial flow of Maxwell fluid, Result Phys 8 (2018) 34–40.

[33] N. Sandeep, C. Sulochana, Dual solutions for unsteady mixed convection flow of MHD micropolar fluid over a stretching/shrinking sheet with non-uniform heat source/sink, Eng. Sci. Tech. Int. J. 18 (2015) 738–745.

[34] S. Rosseland, Astrophysik und Atom-TheoretischeGrundlagen, Springer Verlag, Berlin, 1931, pp. 41–44.

[35] S. Seigel, J.R. Howell, Thermal Radiation Heat Transfer, second ed., Mc Graw Hill Inc, New York, 1981.

https://doi.org/10.1016/j.heliyon.2019.e01465

[36] A. Pantokratoras, T. Fang, Sakiadis flow with nonlinear Rosseland thermal radiation, Phys. Scripta 87 (1) (2012), 015703.

[37] M. Mustafa, J.A. Khan, Numerical study of partial slip effects on MHD flow of nanofluids near a convectively heated stretchable rotating disk, J. Mol. Liq. (2017).

[38] T. Hayat, M. Ijaz, S. Qayyum, M. Ayub, A. Alsaedi, Mixed convective stagnation point flow of nanofluid with Darcy-Fochheimer relation and partial slip, Results Phys 9 (2018) 771−778.

https://doi.org/10.1016/j.heliyon.2019.e01465